BULLETIN OF THE POLISH ACADEMY OF SCIENCES
TECHNICAL SCIENCES
Vol. 55, No. 2, 2007

X-ray microdiffraction on flow-controlled biomolecular assemblies

H.M. EVANS[1], R. DOOTZ[1], S. KÖSTER[1], B. STRUTH[2], and T. PFOHL[1*]

[1]Max Planck Institute for Dynamics and Self-Organization, Bunsenstr 10, D-37073 Göttingen, Germany
[2]European Synchrotron Radiation Facility, 6 Jules Horowitz St., BP 220, 38043 Grenoble Cedex, France

Abstract. The study of liquid crystalline assemblies, with an emphasis on biological phenomena, is now accessible using newly developed microdevices integrated with X-ray analysis capability. Many biological systems can be described in terms of gradients, mixing, and confinement, all of which can be mimicked with the use of appropriate microfluidic designs. The use of hydrodynamic focusing creates well-defined mixing conditions that vary depending on parameters such as device geometry, and can be quantified with finite element modelling. We describe experiments in which geometry and strain rate induce finite changes in liquid crystalline orientation. We also demonstrate the online supramolecular assembly of lipoplexes. The measurement of lipoplex orientation as a function of flow velocity allows us to record a relaxation process of the lipoplexes, as evidenced by a remarkable 4-fold azimuthal symmetry. All of these processes are accessible due to the intentional integration of design elements in the microdevices.

Key words: X-ray diffraction, hydrodynamic focusing, DNA, microfluidic, self-assembly, lipoplex.

1. Introduction

The use of microfluidic tools has enabled a wealth of new technologies, ranging from combinatorial chemistry to biological assays [1–4]. New developments arise from the myriad advantages of fluid flow on the micrometer scale, namely reduced sample volumes, higher efficiencies, and easily adapted designs. The use of soft lithography, typically involving an elastomer such as polydimethylsiloxane (PDMS), has significantly contributed to these advances in technology because of its ease of use [5]. Structures are readily designed to meet a variety of experimental demands. Apart from the obvious engineering advantages provided by such microfluidic tools, however, new access is gained to the fundamental study of materials in flow [6]. This includes both the supramolecular interactions of multiple components, such as enzyme kinetics [2,7], as well as the study of single molecules, such as the fibrous protein actin. A wide variety of chemical environments are easily created using a gradient of reactants in some cases, or by immediate mixing in other cases. Remarkably, non-equilibrium dynamics are accessible in steady-state flow.

Biomaterial investigations in particular benefit from microfluidic technologies [8,9]. This is in part a question of length scale: many biopolymers such as DNA and actin have lengths on the order of micrometers. In addition, the self-assembly of biomaterials is often induced by the presence of enzymes and other proteins, salts, and pH changes. These environments can be created in a controlled manner using a suitable microfluidic device. Several examples of possible microdevice scenarios mimicking cellular phenomena are given in Fig. 1. For example, dense intracellular protein networks result in a confining effect on single embedded protein fibers. In the lab, microchannel dimensions can be tuned in order to mimic this environment.

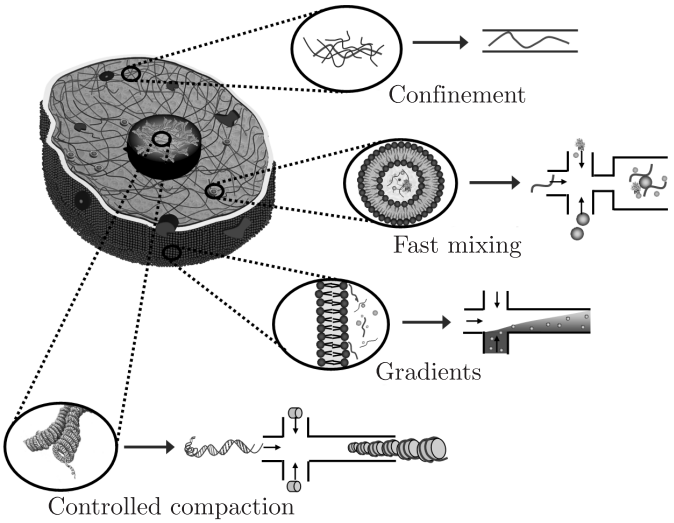

Fig. 1. Examples of the manner in which cellular phenomena (encircled) can be mimicked using microfluidic techniques (arrow). From top: dense protein matrices confine single fibers; fast mixing in lysosomes; chemical gradients across the plasma membrane; chromosomal compaction of DNA

Fast mixing conditions in these devices are also accessible. A biological example of fast mixing reactions is within lipid vesicles called lysosomes, which are responsible for the degradation of organelles and play a vital role in the cycling of materials in and out of the cell. The chemical

*e-mail: thomas.pfohl@ds.mpg.de

gradients across plasma membranes may also be approximated by utilizing well-defined concentration ascents in microflow conditions. In addition, hierarchical assemblies of biomaterials, such as the compaction of DNA into chromosomes, can also be recreated within microchannels. The subsequent dynamic evolution of DNA mesophases is then experimentally accessible. Investigations of biomaterials in microchannel devices allow researchers to isolate key elements of biological processes in a well-defined ambient environment. Causal relationships and kinetic rates can be probed, and unanswered questions regarding underlying principles of assembly or biomaterial function can be examined. With the appropriate knowledge of initial conditions, the concentration and velocity gradients within microdevices can be predicted using finite element modeling (FEM). This has already been shown in the case of collagen, a ubiquitous extracellular protein that forms fibrils 'in vitro' as a function of pH [10].

An additional benefit of studying biomaterials in confining microchannels is the resulting orientation that occurs. These materials often have liquid crystalline properties; therefore, oriented samples can impart additional knowledge with respect to the two- or three-dimensional liquid crystalline phases they form having quasi long-range positional or orientational order. Optical microscopy is a powerful tool for the study of single molecules in micro-scale confinement [11]. However, the use of X-ray diffraction has distinct advantages for investigations probing mesoscale assemblies, because a two-dimensional X-ray pattern illuminates the details of molecular order on commensurate length scales. Small or microfocused X-ray beams are required in order to properly access finite assembly or reaction points in microdevices. The technique was demonstrated in groundbreaking studies of protein folding [12,13]. It is now possible to conduct 'in situ' measurements using microflow devices [14–16], albeit using new strategies for device fabrication such as those elaborated here. The use of flow to align materials as well as isolate interactions of reactants is also advantageous in terms of X-ray measurements. Typically, biomaterials are sensitive to the high energy of X-rays and can rapidly degrade when exposed to a beam for long periods of time. Measurements in microdevices eradicate this concern, because while the X-ray beam remains at a fixed position, the materials within the device continue to flow.

We discuss a new technology using microflow devices together with X-ray microdiffraction. We demonstrate the power of this combination using the liquid crystal 8CB, which shows distinct orientation and restructuring behavior under flow in specially designed microflow devices. We also report the 'in situ' formation of non-viral gene carriers consisting of cationic liposomes. The structural properties of these liposome-DNA assemblies (lipoplexes) have been correlated with their ability to transfer genes, with applications to the field of gene therapy [17].

2. Experimental setup

2.1. Materials. The liquid crystal 8CB (4'-n-octyl-4-cyanobiphenyl) was used as purchased (Sigma Aldrich). The chemical structure is given in Table 1. DNA solutions were prepared by hydrating lyophilized highly polymerized calf thymus DNA (Sigma Aldrich) in 18.2 MΩ Millipore water to a final concentration of 5 mg/mL. The cationic lipid DOTAP (dioleoyl-trimethyl-ammoniumpropane) and the neutral lipid DOPC (dioleoyl-phosphatidylcholine) were mixed 1:1 in chloroform (Avanti Lipids, shown in Table 1). The resulting mixture was dried under a stream of nitrogen, resuspended in water, and hydrated for 12 hours at 37°C. A 25 mg/mL solution of small unilamellar vesicles (diameter less than 200 nm) were formed using an ultrasonic bath.

Table 1. Chemical structures of compounds

Name	Structure
8CB	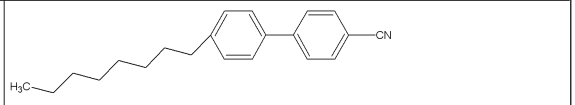
DOPC	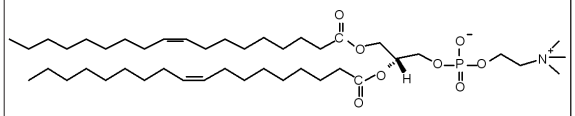
DOTAP	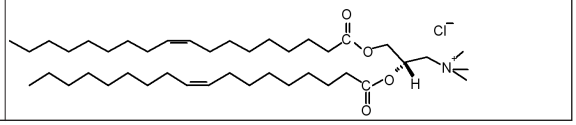

A negative photoresist (SU-8, Micro Resist Technology GmbH) was used in conjunction with standard soft lithography processes reported elsewhere [18]. Poly(dimethysiloxane), PDMS (Sylgard 184, Dow Corning), was mixed with crosslinker in a 10:1 ratio. Kapton adhesive foils were used as received (Dr. Müller GmbH). A custom built pumping system was connected to the microdevices. For the experiments using 8CB, the liquid crystal was pumped in each of 3 inlets at flow rates 10–100 μm/s. The experiments using DNA and lipids had velocities of v_{DNA} about 100 μm/s and lipid velocities v_{lipid} described in the text.

FEMLab software (Comsol, Inc.) was used to perform finite element modeling simulations of conditions within the microchannel device. The incompressible Navier-Stokes equation was solved in two dimensions using about 20.000 elements. Estimates of initial velocity, diffusion, and viscosity are required inputs for the calculations; details of the simulations in Fig. 2 are given in the text.

X-ray measurements conducted using the in-house setup used a Bruker AXS Nanostar setup equipped with a 2D Hi-Star detector and X-ray absorption scanning capability, operated at 4.05 kW (CuK^{α} radiation, $\lambda = 1.54$ Å). Synchrotron experiments were conducted at beamline ID10B at the European Synchrotron Radiation Facility (ESRF) in Grenoble, France. This beam of 8 keV ($\lambda = 1.55$ Å) was focused using compound refractive lenses (CRL) [19] and images were acquired with a CCD camera and a fluorescent screen.

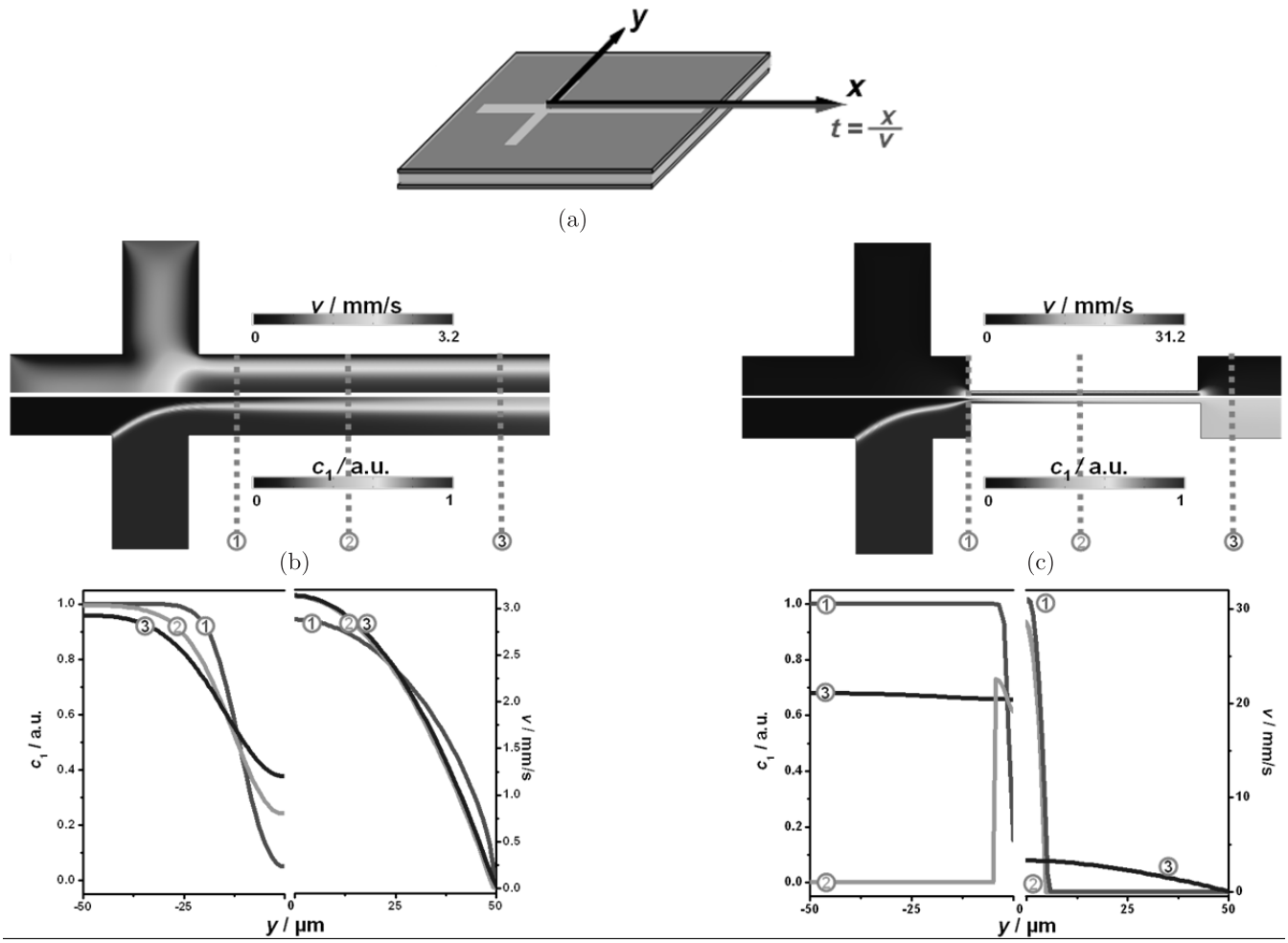

Fig. 2. (a) Positions in the device are described by (x, y) where x is along the interaction channel and y is perpendicular to x. Different time points t can be defined in x along the interaction channel. FEM simulations of velocity v (top) and concentration of side channel component c_1 (bottom) illustrate the effect of (b) laminar mixing in a microchannel, or (c) fast mixing in a stepped channel. Corresponding line profiles of v and c_1 at positions 1–3 are plotted below each of the simulation sets

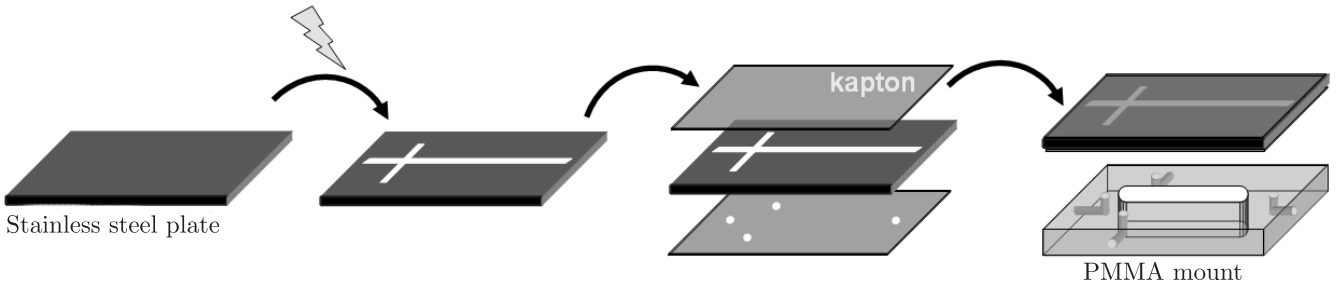

Fig. 3. Production of stainless steel microflow devices

2.2. Microfluidic principles. Coordinates x, y can be defined within a microchannel device, where $x = y = 0$ is defined as the center of two crossed channels (Fig. 2a) for a typical setup. A spatio-temporal relationship along the interaction channel enables studies of time-dependent processes and the isolation of particular time points in a reaction. Hydrodynamic focusing, which can be used to introduce an additional confinement within the interaction channel, is achieved using perpendicularly crossed channels [20]. The details of subsequent mixing between fluids vary greatly depending on the microdevice geometry in the interaction channel.

Two possible mixing scenarios are shown in Fig. 2. One device results in a diffusion limited gradient of the channel components, and the other creates a rapidly mixed solution. Both devices consist of two perpendicularly crossed microchannels, but the inclusion of an immediate stepped decrease in the width of the interaction channel (Fig. 2c) creates markedly different flow conditions than those in a straight channel having constant width (Fig. 2b).

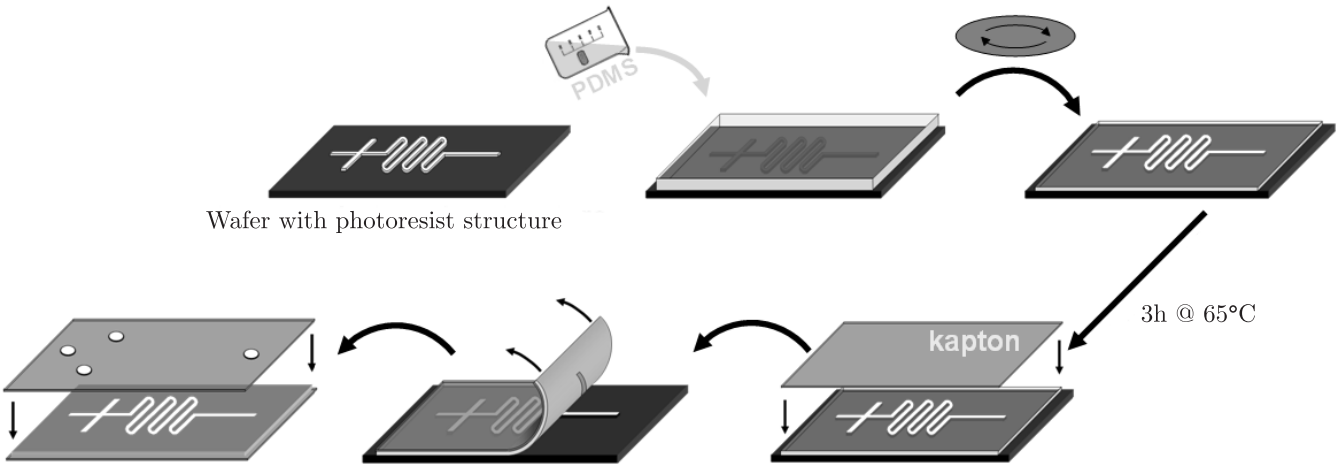

Fig. 4. Fabrication of Kapton-PDMS-Kapton microflow foils

The device shown in Fig. 2b can be used for studies of non-equilibrium structure formation, since each observation point contains a different concentration of reactants. In contrast, the device described in Fig. 2c is useful to quantify the time-evolved properties of a fully mixed ensemble.

The conditions in the two types of microdevices are calculated using FEM. In each device the initial velocities and concentrations are identical. The simulations describe the velocity field and mixing of a side channel component of concentration c_1, which contains small molecules of hydrodynamic radius $r_{\text{water}} = 4.5$ Å and diffusion constant $D = 5 \cdot 10^{-10}$ m^2/s. These values are comparable to those of small biologically relevant molecules such as glucose. The initial velocities of the aqueous solutions (both having the viscosity of water) from the main and side channels is fixed as $v_0 = 700$ μm/s. Simulations of the velocity field v (top) and concentration of side channel component c_1 (bottom) are shown for each design in Figs. 2b and 2c. However, the scale of v is 10-fold higher for the device in Fig. 2c due to the rapid increase in v in the narrow channel region. In both scenarios, values of c_1 range from $c_1 = 0$ to $c_1 = 1.0$.

Lines crossing the channels quantify the values of v and c_1 at different x positions 1, 2, and 3 (plots in Figs. 2b and 2c). The mixing in the device shown in 2b is a consequence of the laminar flow and diffusion within the channel. A continual increase in c_1 at the channel centre ($y = 0$) is recorded, and will approach a constant value at some further point x when the side and main components are completely mixed. Velocity profiles of this device approach a steady-state value. On the other hand, the device shown in Fig. 2c has extremely steep v and c_1 values moving from the center of the channel outward along the y-axis, when the x position is near the beginning of the channel step (position 1). The fast mixing induced by the limited microchannel geometry results in a nearly constant value of c_1 at positions after the confined region (i.e. position 3).

The two scenarios in Fig. 2 only serve as examples. Interactions within the microchannel can also be controlled by variables such as relative flow velocity and further geometric modifications. Clearly, a wide variety of parameters are sufficiently malleable to enable investigations of real-time dynamic interactions. Furthermore, these parameters may be tailored to address specific experimental systems.

2.3. Microflow devices. We report two types of X-ray compatible microflow devices. Each is able to withstand high flow rates and pressures, and is useful for X-ray applications due to the incorporation of Kapton, a polyimide that has very low absorption of X-rays and does not scatter X-rays within the accessible range of our experiments.
Stainless steel cross channel device. One design for an X-ray microflow device consists of two perpendicular oriented microchannels. The production is illustrated in Fig. 3. These channels (100–150 μm wide) are spark eroded in thin stainless steel plates of depth ranging from 200 to 300 μm. Adhesive Kapton is placed on both sides of the steel plate, such that the material seals the device and serves as a window to the microchannel. After punching holes in one piece of the Kapton, the device is mounted to a slab of PMMA which supports the steel plate and assists with connections to the fluid pumping system.
Kapton-PDMS-Kapton. Another type of microflow device has been created using only PDMS and Kapton foils. The fabrication of these devices is shown in Fig. 4. Microdevice fabrication for the Kapton-PDMS-Kapton foils begins with a silicon wafer, which is spin coated with SU-8 negative photoresist (Micro Resist Technology GmbH). The photoresist is subsequently exposed to a lithography photomask, then crosslinked under UV light. After a post-exposure bake, the wafer is rinsed in SU-8 developer and finally cleaned with isopropanol. In order to create a microdiffraction device, PDMS is spin coated atop the master and excess PDMS is gently scraped off manually. The PDMS elastomer is subse-

quently crosslinked for three hours at 65°C. In the final step of production, Kapton adhesive foils are used to seal the device. Connections to a homebuilt pumping system are easily incorporated by punching holes at the inlet and attaching modified press fitting clamps.

The Kapton-PDMS-Kapton microfoils are a sophisticated addition to the field of microfluidic microdiffraction. This design has several advantages: firstly, the device is made using a silicon/photoresist master that can be reused multiple times. Secondly, the exclusive use of soft materials such as Kapton and PDMS creates a flexible yet robust device. The incorporation of geometric confinements, such as zig-zag profiles or hyperbolic sections, is accomplished using the appropriate lithography film at the stage of master production. The dimensional limits of the Kapton-PDMS-Kapton microfoils are in principle conferred only by our soft lithography techniques, i.e. 1 to 300 micrometers. In-house experiments have demonstrated the successful use of a microfoil of thickness only 35 micrometers (results not shown). Another advantage of this design is the rapid production time and the surprisingly strong adhesion between layers. We have successfully pumped fluids having viscosities on the order of 10,000 mPa/s.

2.4. X-Ray microdiffraction. The experimental setup for a typical microdiffraction study is schematically drawn in Fig. 5. An incoming X-ray beam is focused down to a size commensurate with the microchannel width (for better experimental resolution, ideally the beam is as small as possible). The principle is the same for both synchrotron as well as in-house setups. Using synchrotron radiation, a set of compound refractive lenses is incorporated [19,21]. The use of these lenses results in a final beam diameter of 20 μm. In contrast, the final spot size of X-rays using an in-house anode source is 200 μm due to the incorporation of pinholes. The microflow device is placed in the beam path and connected to an external pumping system as well as an $x-y$ stage. The microdevice is moved along coordinates x, y such that the X-ray beam passes through the desired position in the device. An image is collected using either a fluorescent screen and CCD camera (synchrotron) or multi-wire camera (in-house).

A typical two-dimensional X-ray image shows rings of intensity corresponding to features of the liquid crystalline lattices that are probed. The real spacing d of these features is inversely proportional to the momentum transfer $q = 4\pi/\lambda \sin\theta$, where λ is the X-ray wavelength and 2θ is the angle between incident and scattered radiation. A plot of intensity versus q is obtained by radially averaging the image over 360°. As an example, Fig. 6a shows a 2-dimensional image and the resulting plot of intensity versus q for the liquid crystal 8CB (also discussed in section 3). The q ranges accessed in the experiments described in this paper range from 0.025–0.35 Å^{-1}, corresponding to lattice spacings on the order of 20–250 Å. In the event that multiple peaks are collected, the relationship between the q positions can help to elucidate the exact lattice (i.e. lamellae, as seen in Section 4).

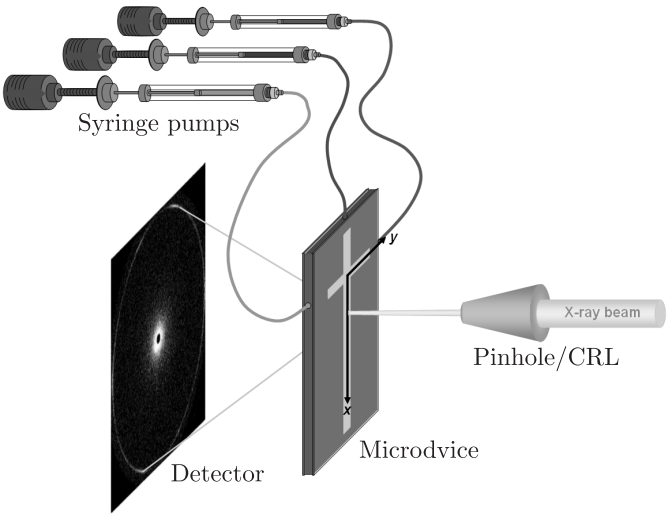

Fig. 5. X-ray microdiffraction setup. The incoming X-ray beam is focused using CRLs (synchrotron) or pinhole apertures (in-house). A fixed position x, y in the microdevice is probed and a resulting 2D image is collected at the detector. Flow in the device is controlled with a custom built pumping system

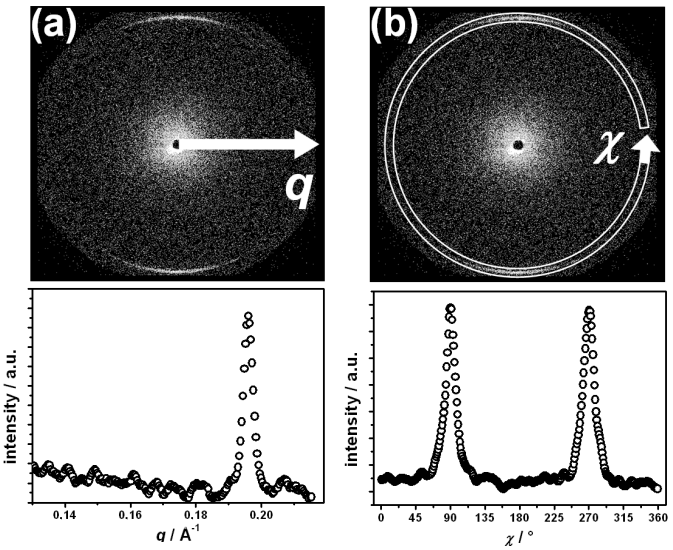

Fig. 6. A demonstration of X-ray diffraction principles using the liquid crystal, 8CB. (a) Radial averaging of the image over all azimuthal angles (top) results in a plot of intensity versus scattering vector q. (b) Azimuthal integration of a raw image (top) about a fixed radial position results in a plot of intensity versus orientation angle χ

The azimuthal distribution of peak intensity is also a quantity of interest, particularly because the alignment of materials occurs in microflow. The materials investigated here are not single crystalline, and their 2-dimensional scattering images reflect a powder average from multiple orientations. This results in intensity values along a ring at fixed radial position q. As is demonstrated in Fig. 6b, a plot of intensity versus the azimuthal angle χ is obtained

by integrating azimuthally ($\chi = 0° - 360°$) along a fixed q. In addition, the orientation parameter $\Delta\chi$ (defined as the full width at half maximum of a peak in such a plot) is a useful value to quantify the extent of material orientation within the microdevices.

3. Liquid crystal behaviour in confining geometries

The liquid crystal 8CB is a thermotropic liquid crystal and forms layers displaying a smectic A liquid crystalline phase at room temperature [22]. The smectic layers of 8CB have a spacing $d = 31.7$ Å, which is easily accessible by the X-ray microdiffraction setups. This is readily seen in Fig. 6a, which contains a plot of scattered intensity versus momentum transfer $q(q = 2\pi/d)$, where $q = 0.198$ Å^{-1}. In addition, the mesoscale assembly of 8CB molecules is strongly influenced by geometric constraint [23,24]. Therefore, this liquid crystal was chosen to demonstrate the utility of microflow foils.

The experiments with 8CB were conducted using a Kapton-PDMS-Kapton device that has several unique features. The channel length has been extended in a serpentine manner to lengthen the residence time of molecules. Coincidentally, wide bending regions are introduced. This is seen schematically in Fig. 7, which shows the entire device as well as a close-up of one bend. The fluid streamlines are shown with arrows. The orientation of 8CB layers is induced by the geometry of the curve. This can be seen in the 2-dimensional scattering images at positions 1–5 that follow the bend, given in Fig. 7. Additionally, azimuthal χ integrations along the diffraction peaks at position q quantify the process of layer reorientation. The orientations at the initial (1) and final (5) positions are indistinguishable due to the symmetry of the layers.

The same microflow device also incorporates sections where the channel geometry is hyperbolic and the width of the channels decreases from 150 μm down to 50 μm. A FEM simulation of the velocity field in one hyperbolic region of length 2 mm is shown in Fig. 8a, along with arrows conveying the magnitude of velocity per position. The geometry has a specific advantage in terms of the fluid flow within the device: the velocity increases and decreases along the channel in a linear fashion. This is seen in Fig. 8d, where the velocity is plotted against position x along the middle of the channel. The mechanical implications of this linear velocity increase stem from the fact that the strain rate is described as the gradient of the velocity, $\dot{\varepsilon} = \partial v/\partial x$. It follows that a constant strain rate exists in the hyperbolic channel, with a change in sign occurring at the midpoint of the channel, $\dot{\varepsilon} = 0$ (Fig. 8c).

A higher degree of orientation of 8CB layers is seen in the hyperbolic region, where the strain rate has a maximum value. This orientation parameter is defined as $\Delta\chi$, the full width at half maximum of the diffraction peak q when integrated azimuthally along χ. A smaller value $\Delta\chi$ therefore corresponds to a narrower distribution of 8CB layer orientations. A steep decrease in $\Delta\chi$ occurs at positions approaching the center of the hyperbolic region, $x = 0$. Values of $\Delta\chi$ along the microchannel are shown in Fig. 8b. The orientation parameter $\Delta\chi$ recedes to its initial value at further positions x as the hyperbolic channel once again widens. Additionally, the asymmetry of the $\Delta\chi$ values around $x = 1$ mm provides insights into the behavior of liquid crystalline materials under shear stress. The 8CB layers return to their original value at a slower rate than the rate at which they ordered, thus suggesting a relaxation process.

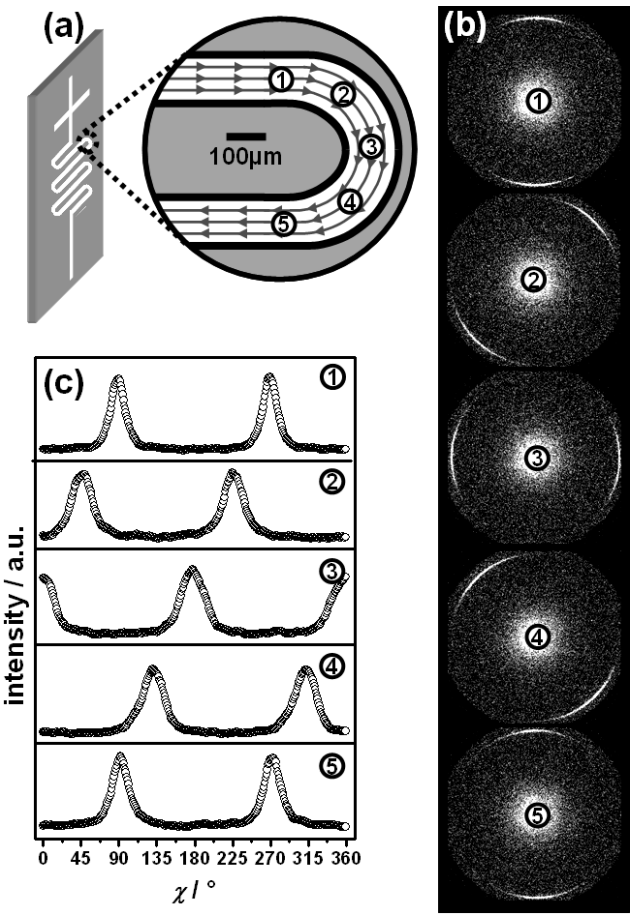

Fig. 7. (a) A long-lifetime Kapton-PDMS-Kapton device consists of many bended regions. The effect of the channel geometry is to reorient 8CB layers, as seen in the raw image data (b) and corresponding χ plots (c) for positions 1–5 along the bend

Another feature shown in Fig. 8b is a slight increase in $\Delta\chi$ at the two endpoints of the hyperbolic region, $x = 0$ and $x = 2$ mm. This increasing disorder is a consequence of the transition between straight channel edges and curved edges. The 8CB layers exist in discretely oriented domains on the micrometer length scale [18,25]. The microdomains, illustrated in Fig. 8e for the channel position $x = 2$ mm, are forced to adapt to the streamlines within the microdevice. However, due an averaging effect

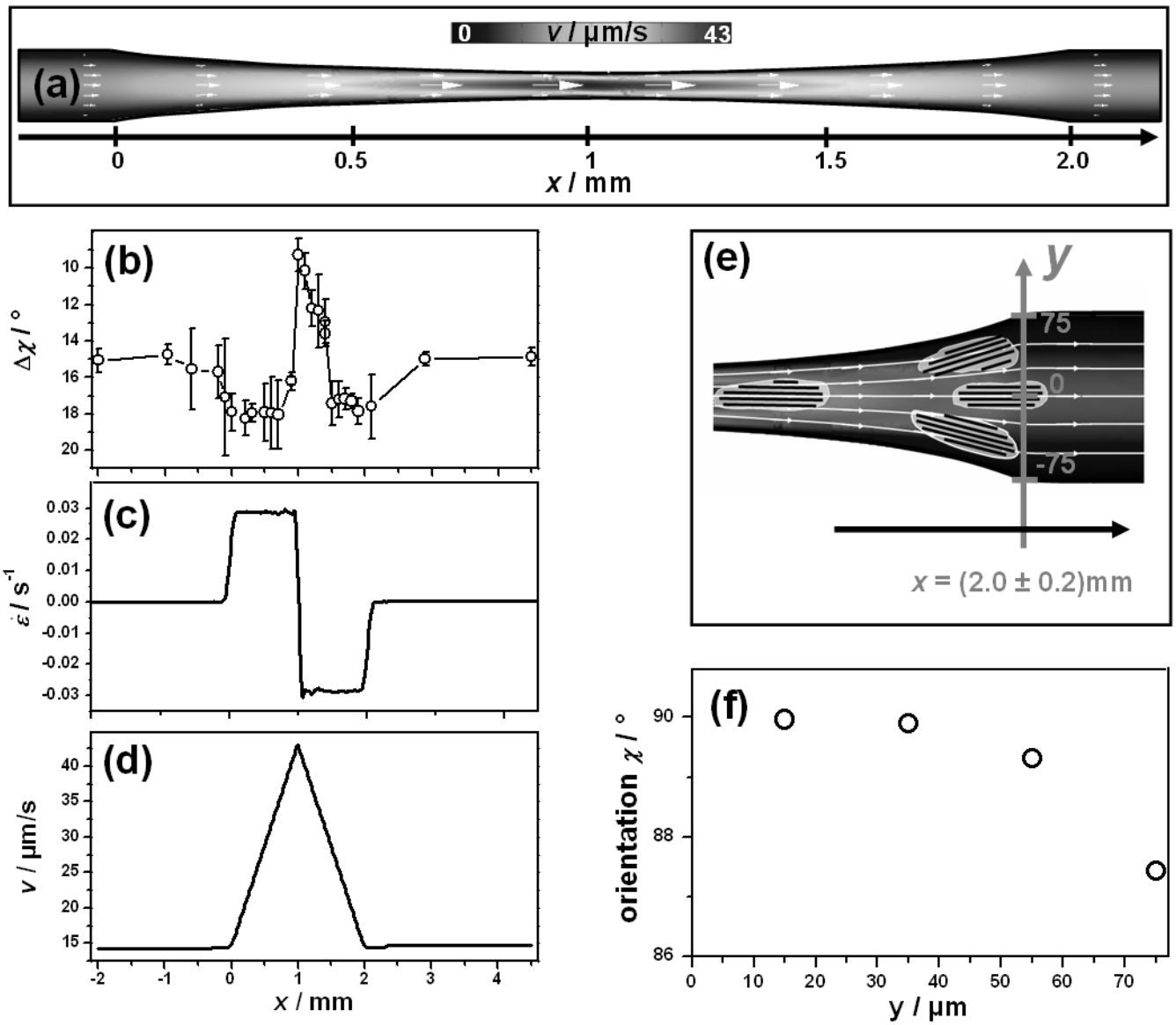

Fig. 8. The velocity profile in a hyperbolic region (a) is linear in position x (d) resulting in a constant strain rate $\dot{\varepsilon}$ (c). The orientation parameter $\Delta\chi$ of 8CB diffraction peaks within the channel has a minimum value at $x = 1$, indicating the highest 8CB layer orientation at the channel midpoint (b). The smaller synchrotron beam size enables the visualization of tilted 8CB microdomains (f) at the juncture where the hyperbolic region begins (shown with velocity profile and y axis in e)

of the large in-house X-ray beam diameter of 200 µm, the gradient of microdomain orientations is not discernible and results in higher total $\Delta\chi$ values. In contrast, experiments using synchrotron radiation (beam diameter of 20 µm) are able to isolate the changes in orientation near the edges of the microdevice. Specific measurements of χ from the center of the channel at $y = 0$ µm to $y = 75$ µm (at the edge of the channel) are given in Fig. 8f.

These experiments lay a foundation for future experiments involving biomaterials. The same principles demonstrated with the 8CB system (i.e. alignment in shear fields and confining geometries as well as induced rotation) can be measured with liquid crystalline biological matter. For example, DNA is a long chain polymer that exhibits a variety of well-known liquid crystalline phases [26]. The behavior of DNA in flow has already been investigated using straight channel geometries [14], and such studies will benefit greatly by the incorporation of these new Kapton-PDMS-Kapton microflow foils.

4. 'In situ' formation of non-viral gene delivery vectors

The promise of gene delivery as a viable method to cure or treat diseases has not yet been attained, and in fact recent attempts to deliver therapeutic DNA using viruses resulted in the death of a patient [27]. Alternative non-viral techniques incorporate materials such as liposomes, in the hope that they can mimic the behavior of viruses [28]. To improve their therapeutic efficiency, attempts have been made to correlate the structure of these materials with

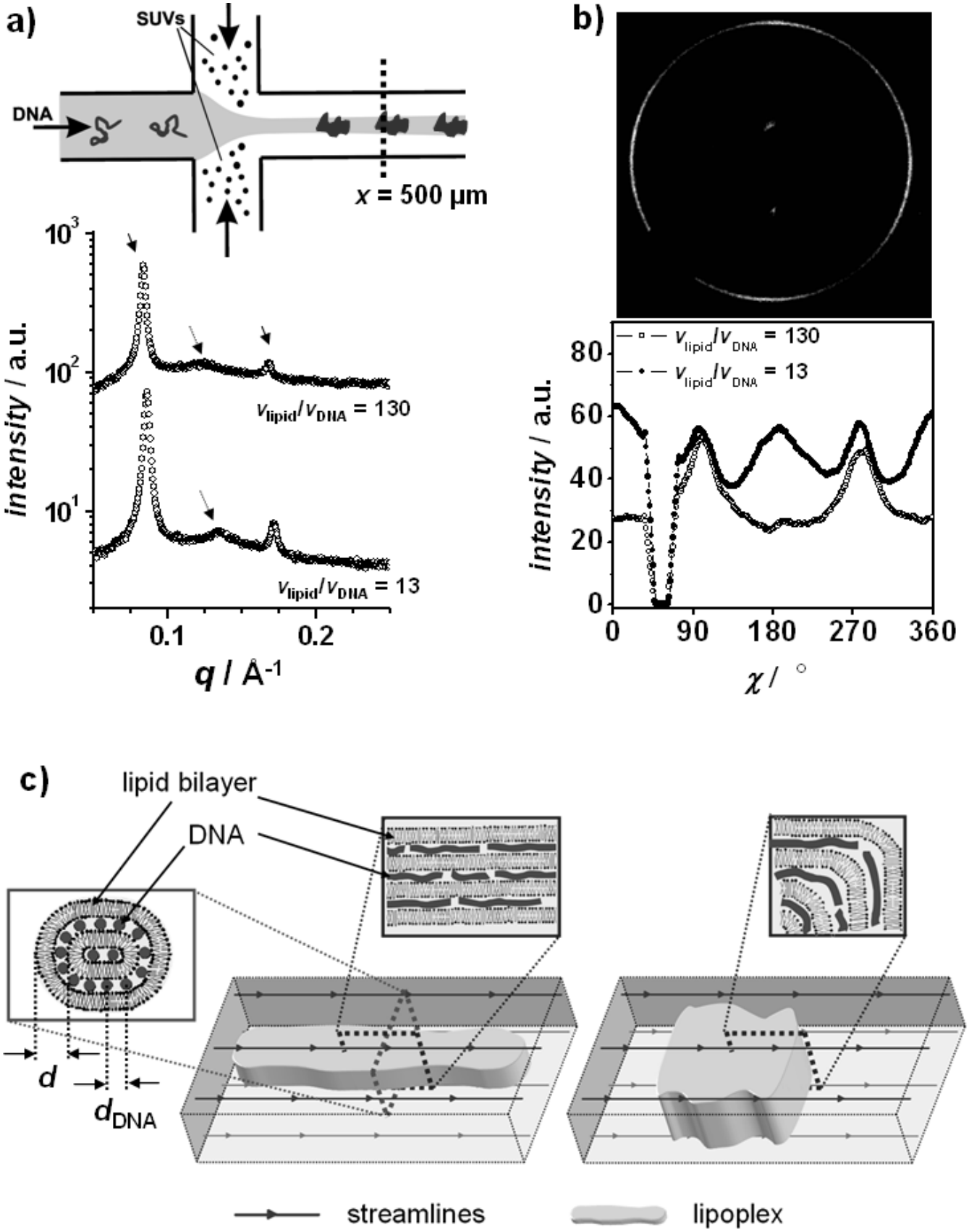

Fig. 9. (a) Formation of lipoplexes in microchannels is achieved by hydrodynamically focusing DNA with side channels containing SUVs (top). SAXS (bottom) reveals two diffraction peaks (arrows) confirming the formation of multilamellae. The dashed arrow corresponds to spacing of intralayer DNA rods. (b) Diffraction image for the case in which four maxima in χ are seen (top). Orientation χ of lipid diffraction peak for two velocities $v_{\mathrm{Lipid}}/v_{\mathrm{DNA}}$ (bottom). (c) Proposed mechanism of perpendicular ordering of lipoplex in flow

their biological performances. The identification of lipid-DNA mesophases using X-ray diffraction has been shown, in some cases, to predict their biological success in an 'in vitro' gene delivery system [29,30]. However, high quantities of novel lipids are not usually available. The formation of lipoplexes in flow on micrometer length scales drastically reduces the amounts of required materials. This is a compelling argument for adopting the schema described here for future structural studies of lipoplexes containing newly designed lipids.

The experimental setup, employing a steel microdevice, is sketched in Fig. 9a (top). The incoming stream of DNA is hydrodynamically focused by side channels of cationic small unilamellar vesicles (SUVs), and the self-assembly of the liposomes and DNA is monitored downstream. The spontaneous formation of lipoplexes requires a physical description. Cationic lipids are incorporated into liposomes, such that the overall charge is positive. The complexation of cationic liposomes and negatively charged DNA is spontaneous and driven by entropy gain and counterion release [31]. The formation of multilamellar lipoplexes is revealed by scattering features at three values of q in X-ray images acquired at device position $x = 500$ μm (Fig. 9a) [31]. This diffraction pattern is unique to an assembly of both lipid and DNA. This claim is verified by X-ray measurements at the device inlet positions, which show no scattering in the same q-range (results not shown). Two peaks q_0 and q_1 (solid arrows in Fig. 9a) are related as $q_1 = 2 \cdot q_0$, corresponding to a multilamellar lattice of spacing $d = 2\pi/q_0 = 72$ Å. This distance d is the sum of the lipid bilayer thickness plus the thickness of water between membranes. Another feature, seen at an intermediate q position (dashed arrow in Fig. 9a), corresponds to an intralayer DNA-DNA correlation. DNA strands are organized in the water region between lipid membrane layers with a characteristic center-to-center distance of $d_{\mathrm{DNA}} = 2\pi/q_{\mathrm{DNA}} \sim 50$ Å. The two length scales are illustrated in the cross-sectional view of Fig. 9c.

The self-assembly of DNA-lipid complexes is achieved at two different flow ratios $v_{\mathrm{lipid}}/v_{\mathrm{DNA}}$. In both cases v_{DNA} is fixed; therefore the higher flow ratio also corresponds to higher flow velocities. A small increase in q_{DNA} is observed when the flow ratio is lower. This change reflects a slight reorganization of DNA rods in the lipoplex over time, from $d_{\mathrm{DNA}} = 50$ Å to $d_{\mathrm{DNA}} = 47$ Å [15]. Our results indicate that the rearrangement of SUVs and DNA strands occurs on two time scales: firstly, the initial reorganization into a multilamellar-sandwich occurs, and secondly the DNA strands find the most favourable DNA-DNA distance. The experimental setup described here uniquely enables the visualization of both events. The spacings obtained using our setup agree with bulk capillary measurements reported by Rädler et al. [31]. In our case, however, we access the real time dynamic complexation and optimization of lipid and DNA lipoplexes.

An interesting effect of flow velocity is highlighted in Fig. 9b. The azimuthal χ integrations are shown for peaks q_0 from Fig. 9a. (Zero values correspond to the beam stop position and are irrelevant.) As a reminder, the peak at q_0 corresponds to a multilamellae repeat spacing. We find that the majority of scattering from multilamellae along radial position q_0 is distributed at azimuthal angles $\chi = \pm 90°$ at both $v_{\mathrm{lipid}}/v_{DNA}$ ratios. This orientation is coincident with the flow direction in the microchannel. However, two additional azimuthal intensity maxima at $\chi = \pm 180°$ are recorded at the slower velocity, when $v_{\mathrm{lipid}}/v_{DNA} = 13$ (Fig. 9b, top). These maxima indicate an orientation that is exactly transverse to the direction of flow. A similar phenomenon was reported for nematic liquid crystals, although the nature of the orientation was not clear [32]. In our system, we explain this transverse orientation in terms of a relaxation process of the lipoplexes. It is important to note that the 4-fold χ orientation is seen only at the slower flow velocity. For both flow speeds, the measurements reported here were acquired at $x = 500$ μm in the device ($x = 0$, as always, is defined as the center of the cross). In general, we expect that the strain rate $\dot{\varepsilon}$ acts to extend the lipoplexes along the flow direction (see Fig. 9c). For both flow velocity ratios, the device region of maximum $\dot{\varepsilon}$ occurs at a point preceding our measurement in the device. However, although the observation position is fixed, it corresponds to different time scales for the two velocities. The subsequent relaxation of lipoplexes is only observable at $v_{\mathrm{lipid}}/v_{DNA}$ sufficiently slow enough to view the process. These stretching and relaxation events are illustrated in Fig. 9c. The lipoplexes adopt a 'square' reorganization that is likely stabilized due to the length scales and physical properties of the lipid membranes and DNA strands (see Fig. 9c).

5. Concluding remarks

A multitude of possible experimental conditions are attainable using microfluidics. These include the creation of biomimetic setups that emulate biophysical processes such as DNA compaction and biopolymer confinement. Moreover, X-ray diffraction is a useful tool to quantify the liquid crystalline assembly of biomaterials. We therefore develop new strategies to join microfluidics with X-ray diffraction. This is achieved with new specially designed X-ray compatible microdevices. Two types of devices utilize different fabrication methods, but both take advantage of X-ray compatible Kapton adhesive foils.

We describe two different experiments, both demonstrating the effects of mechanically and geometrically induced stresses on complex fluids in flow. First, the geometrically induced orientation of the liquid crystal 8CB is followed at different points in a Kapton-PDMS-Kapton microflow foil. The narrowest azimuthal distribution of layer orientations occurs simultaneously with a maximum in strain rate, which is calculated using FEM simulations. Second, cationic lipid-DNA lipoplexes are formed

in situ using the steel cross microdevice. A reorganization of the supramolecular lipoplex assembly is quantified by a shift in the intralayer DNA spacing d_{DNA}. In addition, we find a remarkable 4-fold azimuthal symmetry corresponding to a post-strain lipoplex relaxation. These results with lipoplexes show the usefulness of microdiffraction in rapidly ascertaining their structure, dimensions, time scales, and responses to mechanical stress. The measurements also benefit from the extremely low sample volumes and on-line amenability of conditions.

The development of these new X-ray compatibile microflow foils now places researchers in an advantageous position to approach important biophysical questions regarding the self-assembly of biomatter and interactions in a variety of environments, such as those illustrated in Fig. 1. Fortunately, the devices described here benefit from facile production methods and robust characteristics. In addition, these microflow foils can incorporate more complex designs, and future experiments will aim to study hierarchical organizations, such as chromosome formation, with the integration of additional inlet channels.

Acknowledgements. We are thankful for fruitful discussions with Stephan Herminghaus, Dagmar Steinhauser, Anatoly Snigirev, and Oleg Konovalov, as well as excellent technical assistance from Udo Krafft and experimental aid from Alexander Otten. ESRF kindly provided beamtime at ID10b. H.E. acknowledges a fellowship from the Alexander von Humboldt Foundation. This work was supported by the DFG within the Emmy-Noether-Program, PF 375/2. The current address of B.S. is HASYLAB at DESY, Notkestrasse 85, D-22603 Hamburg, Germany. All correspondence should be addressed to T.P.

References

[1] G.M. Whitesides, "The 'right' size in nanobiotechnology", *Nature Biotechnology* 21 (10), 1161–1165 (2003).

[2] J. Su, M.R. Bringer, R.F. Ismagilov, and M. Mrksich, "Combining microfluidic networks and peptide arrays for multi-enzyme assays", *J. American Chemical Society* 127 (20), 7280–7281 (2005).

[3] E.P. Kartalov, W.F. Anderson, and A. Scherer, "The analytical approach to polydimethylsiloxane microfluidic technology and its biological applications", *J. Nanoscience and Nanotechnology* 6 (8), 2265–2277 (2006).

[4] Y. Kikutani, M. Ueno, H. Hisamoto, M. Tokeshi, and T. Kitamori, "Continuous-flow chemical processing in three-dimensional microchannel network for on-chip integration of multiple reactions in a combinatorial mode", *QSAR and Combinatorial Science* 24 (6), 742–757 (2005).

[5] J.C. McDonald and G.M. Whitesides, "Poly(dimethylsiloxane) as a material for fabricating microfluidic devices", *Accounts of Chemical Research* 35 (7), 491–499 (2002).

[6] T. Pfohl, F. Mugele, R. Seemann, and S. Herminghaus, "Trends in microfluidics with complex fluids", *Chem. Phys. Chem.* 4 (12), 1291–1298 (2003).

[7] K. Ahn, J. Agresti, H. Chong, M. Marquez, and D.A. Weitz, "Electrocoalescence of drops synchronized by size-dependent flow in microfluidic channels", *Applied Physics Letters* 88 (26) (2006).

[8] D.J. Beebe, G.A. Mensing, and G.M. Walker, "Physics and applications of microfluidics in biology", *Annual Review of Biomedical Engineering* 4, 261–286 (2002).

[9] C. Hansen and S.R. Quake, "Microfluidics in structural biology: smaller, faster, better", *Current Opinion in Structural Biology* 13 (5), 538–544 (2003).

[10] S. Köster, J.B. Leach, B. Struth, T. Pfohl, and J.Y. Wong, "Visualization of flow-aligned type I collagen self-assembly in tunable pH gradients", *Langmuir* 23, 357–359 (2007).

[11] S. Köster, D. Steinhauser, and T. Pfohl, "Brownian motion of actin filaments in confining microchannels", *J. Phys.: Condens. Matter* 17, S4091–S4104 (2005).

[12] L. Pollack, M.W. Tate, A.C. Finnefrock, C. Kalidas, S. Trotter, N.C. Darnton, L. Lurio, R.H. Austin, C.A. Batt, S.M. Gruner, and S.G.J. Mochrie, "Time resolved collapse of a folding protein observed with small angle x-ray scattering", *Physical Review Letters* 86 (21), 4962–4965 (2001).

[13] L. Pollack, M.W. Tate, N.C. Darnton, J.B. Knight, S.M. Gruner, W.A. Eaton, and R.H. Austin, "Compactness of the denatured state of a fast-folding protein measured by submillisecond small-angle x-ray scattering", *Proc. National Academy of Sciences* USA 96 (18), 10115–10117 (1999).

[14] R. Dootz, A. Otten, S. Köster, B. Struth, and T. Pfohl, "Evolution of DNA compaction in microchannels", *J. Phys.: Condens. Matter* 18 (18), S639–S652 (2006).

[15] A. Otten, S. Köster, B. Struth, A. Snigirev, and T. Pfohl, "Microfluidics of soft matter investigated by small-angle X-ray scattering", *J. Synchrotron Radiation* 12, 745–750 (2005).

[16] W.R. Burghardt, E.F. Brown, M.L. Auad, and J.A. Kornfield, "Molecular orientation of a commercial thermotropic liquid crystalline polymer in simple shear and complex flow", *Rheologica Acta* 44 (5), 446–456 (2005).

[17] K.K. Ewert, A. Ahmad, H.M. Evans, and C.R. Safinya, "Cationic lipid-DNA complexes for non-viral gene therapy: relating supramolecular structures to cellular pathways", *Expert Opinion on Biological Therapy* 5 (1), 33–53 (2005).

[18] R. Dootz, H.M. Evans, S. Köster, and T. Pfohl, "Rapid prototyping of X-ray microdiffraction compatible continuous microflow foils", *Small* 3 (1), 96–100 (2007).

[19] A. Snigirev, V. Kohn, I. Snigireva, and B. Lengeler, "A compound refractive lens for focusing high-energy X-rays", *Nature* 384 (6604), 49–51 (1996).

[20] J.B. Knight, A. Vishwanath, J.P. Brody, and R.H. Austin, "Hydrodynamic focusing on a silicon chip: Mixing nanoliters in microseconds", *Physical Review Letters* 80 (17), 3863–3866 (1998).

[21] B. Struth, A. Snigirev, O. Konovalov, A. Otten, R. Gauggel, and T. Pfohl, "Application of microfocussing at a non-specific beamline", *SRI 2003 Proc. AIP Conf. Proceedings* 705, 804 (2004).

[22] D. Davidov, C.R. Safinya, M. Kaplan, S.S. Dana, R. Schaetzing, R.J. Birgeneau, and J.D. Litster, "High-resolution X-Ray and light-scattering study of critical be-

havior associated with the nematic-smectic-A transition in 4-Cyano-4'-Octylbiphenyl", *Physical Review B* 19 (3), 1657–1663 (1979).

[23] T. Pfohl, J.H. Kim, M. Yasa, H.P. Miller, G.C.L. Wong, F. Bringezu, Z. Wen, L. Wilson, M.W. Kim, Y. Li, and C.R. Safinya, "Controlled modification of microstructured silicon surfaces for confinement of biological macromolecules and liquid crystals", *Langmuir* 17 (17), 5343–5351 (2001).

[24] M.C. Choi, T. Pfohl, Z.Y. Wen, Y.L. Li, M.W. Kim, J.N. Israelachvili, and C.R. Safinya, "Ordered patterns of liquid crystal toroidal defects by microchannel confinement", *Proc. National Academy of Sciences* USA 101 (50), 17340–17344 (2004).

[25] S.H.J. Idziak, C.R. Safinya, R.S. Hill, K.E. Kraiser, M. Ruths, H.E. Warriner, S. Steinberg, K.S. Liang, and J.N. Israelachvili, "The X-ray surface forces apparatus – structure of a thin smectic liquid-crystal film under confinement", *Science* 264 (5167), 1915–1918 (1994).

[26] D. Durand, J. Doucet, and F. Livolant, "A study of the structure of highly concentrated phases of DNA by X-ray-diffraction", *Journal de Physique II* 2 (9), 1769–1783 (1992).

[27] S.E. Raper, N. Chirmule, F.S. Lee, N.A. Wivel, A. Bagg, G.P. Gao, J.M. Wilson, and M.L. Batshaw, "Fatal systemic inflammatory response syndrome in a ornithine transcarbamylase deficient patient following adenoviral gene transfer", *Molecular Genetics and Metabolism* 80 (1–2), 148–158 (2003).

[28] P.L. Felgner and G. Rhodes, "Gene therapeutics", *Nature* 349, 351–352 (1991).

[29] A. Ahmad, H.M. Evans, K. Ewert, C.X. George, C.E. Samuel, and C.R. Safinya, "New multivalent cationic lipids reveal bell curve for transfection efficiency versus membrane charge density: lipid-DNA complexes for gene delivery", *J. Gene Medicine* 7 (6), 739–748 (2005).

[30] K.K. Ewert, H.M. Evans, A. Zidovska, N.F. Bouxsein, A. Ahmad, and C.R. Safinya, "A columnar phase of dendritic lipid-based cationic liposome-DNA complexes for gene delivery: Hexagonally ordered cylindrical micelles embedded in a DNA honeycomb lattice", *J. American Chemical Society* 128 (12), 3998–4006 (2006).

[31] J.O. Rädler, I. Koltover, T. Salditt, and C.R. Safinya, "Structure of DNA-cationic liposome complexes: DNA intercalation in multilamellar membranes in distinct interhelical packing regimes", *Science* 275 (5301), 810–814 (1997).

[32] D.K. Cinader and W.R. Burghardt, "X-ray scattering studies of orientation in channel flows of a thermotropic liquid-crystalline polymer", *J. Polymer Science Part B-Polymer Physics* 37 (24), 3411–3428 (1999).